

DifAttack++: Query-Efficient Black-Box Adversarial Attack via Hierarchical Disentangled Feature Space in Cross Domain

Jun Liu¹ · Jiantao Zhou¹ · Jiandian Zeng² · Jinyu Tian³

Received: date / Accepted: date

Abstract This work investigates efficient score-based black-box adversarial attacks with a high Attack Success Rate (ASR) and good generalizability. We design a novel attack method based on a *Hierarchical Disentangled Feature space* and *cross domain*, called **DifAttack++**, which differs significantly from the existing ones operating over the entire feature space. Specifically, DifAttack++ firstly disentangles an image’s latent feature into an *adversarial feature* (AF) and a *visual feature* (VF) via an autoencoder equipped with our specially designed **Hierarchical Decouple-Fusion** (HDF) module, where the AF dominates the adversarial capability of an image, while the VF largely determines its visual appearance. We train such autoencoders for the clean and adversarial image domains respectively, meanwhile realizing feature disentanglement, by using pairs of clean images and their Adversarial Examples (AEs) generated from available surrogate models via white-box attack methods. Eventually, in the black-box

attack stage, DifAttack++ iteratively optimizes the AF according to the query feedback from the victim model until a successful AE is generated, while keeping the VF unaltered. Extensive experimental results demonstrate that our method achieves superior ASR and query efficiency than SOTA methods, meanwhile exhibiting much better visual quality of AEs. The code is available at <https://github.com/csjunjun/DifAttack.git>.

Keywords Black-box Adversarial Attack · Query-Efficient · Disentanglement · Hierarchical

1 Introduction

It has been observed that meticulously crafted Adversarial Examples (AEs) are beneficial for evaluating and improving the robustness of Deep Neural Networks (DNNs) Dong et al (2020); Croce and Hein (2020b). AEs refer to images that deceive DNNs by incorporating imperceptible perturbations onto clean images. The methods for generating AEs can be roughly classified into three categories based on the information of victim DNNs available to the attacker. The first category is the white-box attack Dong et al (2018); Croce and Hein (2020a); Zhang et al (2021), in which the attack method has access to the architecture and weights of the victim model. The second category is called the black-box attack, where the attacker can only obtain the model’s output. The case where the model’s output contains both categories and scores is known as a score-based black-box attack, while the situation where only categories are included is named a decision-based black-box attack Brendel et al (2018). The third category refers to the gray-box attack Guo et al (2018), where attackers can obtain models’ knowledge that falls between white-box attacks and black-box attacks. Given that

Jun Liu¹
E-mail: yc07453@um.edu.mo

Jiantao Zhou¹
E-mail: jtzhou@um.edu.mo

Jiandian Zeng²
E-mail: jiandian@bnu.edu.cn

Jinyu Tian³
E-mail: jytian@must.edu.mo

¹ State Key Laboratory of Internet of Things for Smart City, Department of Computer and Information Science, University of Macau

² Institute of Artificial Intelligence and Future Networks, Beijing Normal University

³ School of Computer Science and Engineering, Macau University of Science and Technology

contemporary potent classification APIs [Google \(2024\)](#); [Imagga \(2024\)](#) generally provide image prediction categories alongside scores, this work primarily focuses on practical score-based black-box attacks.

We observe that current state-of-the-art (SOTA) score-based black-box attack methods predominantly exhibit two aspects that can be improved. **On the one hand**, prior techniques that seek AEs by optimizing image features usually operate within the entire feature space, such as AdvFlow [Mohaghegh Dolatabadi et al \(2020\)](#), TREMBA [Huang and Zhang \(2020\)](#) and CGA [Feng et al \(2022\)](#), without embracing the disentanglement of adversarial capability and visual characteristics in the image feature. Optimizing the entire feature of images perhaps results in substantial pixel perturbations that will encounter truncation by the predefined disturbance constraint, thus diminishing the optimization efficacy of the features and eventually increasing query numbers. Another possible chain reaction is the decrease in the Attack Success Rate (ASR) caused by the limited query numbers. Although there are a few black-box methods that achieve leading ASR and query efficiency, the visual quality of their generated AEs is often unsatisfactory and quite perceptible. For instance, SquareAttack [Andriushchenko et al \(2020\)](#) always produce AEs filled with colored stripes and squares. To improve the unsatisfactory ASR and query efficiency, meanwhile maintaining the visual quality of AEs, our DifAttack++ disentangles an image’s latent feature into an Adversarial Feature (AF) and a Visual Feature (VF), where the former dominates the adversarial capability of an image, while the latter largely determines its visual appearance. Afterward, the AF is iteratively optimized according to query feedback, while keeping the VF unaltered.

On the other hand, some score-based attack techniques including P-RGF [Cheng et al \(2019\)](#) and GFCS [Lord et al \(2022\)](#), exploit the gradients from local white-box surrogate models to update AEs during each query. These methods are effective when image categories of the training dataset for surrogate models and the victim model are the same, namely a **close-set** black-box attack scenario analogy to the close-set recognition setting [Vaze et al \(2021\)](#). When it comes to an **open-set** black-box attack, wherein the training dataset of the victim model is unknown, the effectiveness of these methods declines, as the possible incongruence between the output categories of surrogate models and the victim model hampers the calculation of gradients from surrogate models. Although there are other approaches, such as SimBA [Guo et al \(2019a\)](#), CGA and SquareAttack, which are workable in both the open-set and close-set scenarios. These methods still face challenges in

terms of the query efficiency, ASR or severe degradation of image quality. Our DifAttack++ circumvents the need to compute gradients of surrogate models when updating AEs to be queried. Instead, before embarking upon querying the victim model, we leverage AEs generated by performing white-box attack methods on surrogate models to learn how to extract a disentangled AF and VF from the image’s latent feature, which enables DifAttack++ to more effectively conduct black-box attacks in open-set scenarios. The efficiency of DifAttack++ in open-set scenarios can be attributed to the fact that the disentangled feature space for optimizing AEs is also responsible for the image reconstruction task, which means that an image can still be reconstructed into its original form with minimal loss after being mapped into our disentangled feature space. In contrast, the feature space in other methods, such as TREMBA and CGA, is directly used to generate adversarial perturbations that are tightly bound to the data distribution of the training dataset. The latent feature for image reconstruction in DifAttack++ has better generalizability on unknown datasets than the feature space learned from adversarial perturbation distributions of a specific dataset. In addition, DifAttack++ owns the flexibility to selectively harness surrogate models, e.g., in closed-set scenarios, generating transferable AEs as the starting point for beginning the query attack.

Specifically, in our DifAttack++, we firstly train two distinct autoencoders equipped with our proposed **Hierarchical Decouple-Fusion (HDF)** module to realize image reconstructions and to disentangle AFs as well as VFs from images’ intermediate features. The feature disentanglement is feasible because the adversarial capability is mainly entwined with the decision boundary of classifiers and is relatively independent of the intrinsic image signal, whereas a contrast holds true for the visual appearance. Here, we use two autoencoders with the same architecture but different weights to extract the features of clean images or their AEs separately, since many existing works [Stutz et al \(2019\)](#); [Lin et al \(2020\)](#) have pointed out that regular AEs are off the manifold of clean images. It has also been verified that the Intrinsic Dimensionality (ID) of AEs are larger than clean images in [Qing et al \(2024\)](#), and data with higher ID are more difficult to be modeled by deep learning [Pope et al \(2020\)](#). Therefore, we disentangle clean images and AEs in cross domain for more precise feature representations.

After obtaining well-trained autoencoders, in the attack stage against victim models, we iteratively optimize AFs of perturbed images using the natural evolution strategy [Wierstra et al \(2014\)](#) according to the

query feedback from the victim model, while keeping the VF unaltered, until a successful AE is reconstructed from the fusion of the perturbed AF and the initial image’s VF. The initial image refers to the start point in the attack stage, which is usually set as the clean image in open-set scenarios or a transferable AE in close-set scenarios according to the applicability of surrogate models. More explanations about initial images will be clarified in following Sections. To the best of our knowledge, this is the first work that employs the hierarchical disentangled AFs and VFs in cross domain for black-box adversarial attacks. The contributions of our work can be summarized as follows:

- We design a new hierarchical disentanglement method in cross domain to distill an AF, which has a significant impact on the image’s adversarial capability while minimizing its influence on visual perception, and a VF that has the opposite attributes, from an image’s latent feature;
- Based on this disentanglement, we propose a new black-box attack method, DifAttack++, which generates AEs by optimizing the AF according to the query feedback while maintaining the VF invariant.
- Experimental results demonstrate that DifAttack++ outperforms SOTA score-based black-box attack methods in ASR and query numbers simultaneously in almost all cases, meanwhile maintaining satisfactory visual quality of AEs, both for traditional and large-scale victim models.

Note that an earlier version of DifAttack++, called DifAttack [Liu et al \(2024a\)](#), has been published in AAAI2024. Here we conclude the differences of DifAttack++ from this conference version:

- DifAttack++ designs hierarchical convolution layers for feature disentanglement, considering that one single layer of the decouple-fusion (DF) module in DifAttack may be insufficient to disentangle intensely entangled AFs and VFs.
- Compared to DifAttack, in which clean images and their AEs share the same autoencoder for image reconstruction and feature disentanglement, the use of cross domain in DifAttack++ achieves a more stable and faster training process, meanwhile leading to better more effective attack performance.
- DifAttack uses a clean image to start the attack stage in both close-set and open-set scenarios, but DifAttack++ adopts a transferable AE as the start point in close-set scenarios for extracting more powerful AFs, resulting in better attack performance.

The rest of this paper is organized as follows. Section 2 reviews related works on existing score-based black-box attack methods, together with the development of

disentangled representation. Section 3 introduces the details of our DifAttack++ attack framework, including the train 3.2 and attack 3.3 two stages. Section 4 shows the performance of DifAttack++ and comparison with the competing attack methods in terms of ASR, query efficiency, and visual quality. Finally, Section 5 concludes.

2 Related Works

2.1 Score-based Black-box Attack Methods

As our work mainly focuses on score-based black-box attack methods, we only conduct literature review on such approaches here.

Score-based black-box attack methods can be broadly categorized into three main classes: **transfer-based**, **query-based**, and **query-and-transfer-based** attacks [Feng et al \(2022\)](#). 1) **Transfer-based** approaches query the black-box model once using AEs generated on local surrogate models, as explored in [Qin et al \(2023\)](#) and etc. Such approaches take advantage of the transferability of AEs across classifiers with distinct architectures, but their ASRs generally fall behind query-based attack methods. 2) The **query-based** techniques tackle the black-box optimization through iteratively querying the victim model, including NES [Ilyas et al \(2018\)](#), SignH [Al-Dujaili and O’Reilly \(2020\)](#), \mathcal{N} Attack [Li et al \(2019\)](#), SimBA [Guo et al \(2019a\)](#), etc., which exhibit an augmented ASR compared to transfer-based approaches, albeit demanding a greater number of queries. 3) The **query-and-transfer-based** methods amalgamate the merits of transfer-based and query-based techniques, resulting in an elevated ASR and diminished queries. Certain techniques, such as Subspace [Guo et al \(2019b\)](#), P-RGF [Cheng et al \(2019\)](#), GFCS [Lord et al \(2022\)](#) and BASES [Cai et al \(2022\)](#), update queried AEs by performing white-box attacks against surrogate models with the guidance of the query feedback. Other methods learn adversarial distributions by leveraging pairs of clean images and their AEs obtained by attacking surrogate models, including TREMB [Huang and Zhang \(2020\)](#) and CGA [Feng et al \(2022\)](#), or approximate the adversarial distribution with the clean data distribution, such as AdvFlow [Mohaghegh Dolatabadi et al \(2020\)](#). Then, the learned feature space for mapping the adversarial distribution is adopted as the search space of AEs. Some other approaches incessantly refine an auxiliary model using the query feedback to directly generate AEs [Yin et al \(2023a\)](#), approximate decision boundaries [Yin et al \(2023b\)](#) or gradients [Du et al \(2020\)](#) of victim models, which are time-consuming and resource-intensive.

Notably, MCG Yin et al (2023b) achieves a remarkable ASR and query efficiency by integrating SOTA query-based black-box methods with its proposed meta generator. This generator and surrogate models will be fine-tuned according to query feedback information for adapting to different victim models and test data distributions. More recently, Liu et al (2024b) involves a latest conditional denoising diffusion probabilistic model to learn the transformation from clean images to AEs and then AEs can be directly sampling from this well-trained model.

2.2 Disentangled Representation

In Bengio et al (2013), it is intuitively defined that **Disentangled Representation (DR)** separates the distinct, independent and informative generative factors of variation in the data. Recently, a lot of endeavors have embraced the utilization of autoencoders Hinton and Zemel (1993); Lee et al (2020); Li et al (2023), generative adversarial networks Goodfellow et al (2014); Arora et al (2023); Meo et al (2024), generative flows Ma et al (2020), and diffusion-based models Chen et al (2024); Yang et al (2024) to acquire disentangled representations of data features, for which mutual information Chen et al (2016); Higgins et al (2017); Chen et al (2018); Burgess et al (2018); Kim et al (2021); Lin et al (2021) and total correlation Kim and Mnih (2018); Chen et al (2018); Achille and Soatto (2018); Meo et al (2024) are mostly widely used. Regarding the structure of disentangled features, DR methods can be categorized into dimension-wise and vector-wise Wang et al (2022). Dimension-wise DR methods result in each fine-grained generative factor represented by a 1-dimension scalar in the whole feature representation, while vector-wise DR methods lead to several coarse-grained disentangled factors represented by associated vectors, of which the dimension is larger than two. Our DifAttack++ adopts vector-wise features, which are more suitable for addressing complicated practical tasks. In practical, DR learning has been broadly applied to domain adaption Peng et al (2019); Cai et al (2019), image-to-image translation Gonzalez-Garcia et al (2018); Lee et al (2018a, 2020), person re-identification Choi et al (2020); Wei et al (2023), identity swapping Gao et al (2021), zero-shot recognition Tong et al (2019), subject-driven text-to-image generation Chen et al (2024), and etc.

The usage of DR in the adversarial defense and attack. In the adversarial defense and attack domains involved in this work, DR is commonly harnessed for detecting AEs or improving models' robustness, such as Mustafa et al (2020); Wang et al (2021); Yang

et al (2021a,b); Qing et al (2024). Mustafa et al (2020) class-wise disentangles the intermediate feature representations of classifiers in the training stage, specifically forcing the features of each class to lie inside a convex polytope that is maximally separated from the polytopes of other classes. In Wang et al (2021), a one-off combo-variational autoencoder is applied to disentangling latent codes, making one latent code only affect one semantic feature. This autoencoder is then used for detecting and purifying AEs based on feature manipulation. Yang et al (2021a) trains a variational autoencoder with the help of a classifier to decompose an input image into a part retaining only essential information for classification (i.e. class-essential) and a part covering all the rest redundant information (i.e. class-redundant). Then this work detects the input image as an AE if its kernel density Lee et al (2018b) of class-essential output is below a threshold. Yang et al (2021b) focuses on enhancing classifiers' robustness by training two auxiliary class-specific/-irrelevant classifiers to disentangle class-relevant/-irrelevant features. Qing et al (2024) disentangles the representations of clean counterpart and adversarial perturbations for every input image using several autoencoders, then one of the autoencoders is used for calculate the feature distance between the input image and reconstructed image. Finally, this feature distance is used for detecting whether the input is adversarial.

To the best of our knowledge, only a limited number of *white-box* attack methods have involved feature disentanglement. RNF Kim et al (2021) is a white-box attack approach that optimizes image perturbations by maximizing the gradient of non-robust features in perturbed images, wherein non-robust features are distilled from the target classifier's intermediate features based on information bottleneck Alemi et al (2016). Another white-box attack method Lu et al (2021), called SSAE, trains an autoencoder to directly generate target models' AEs. Its training loss aims to minimize the norm difference of output logits between clean images and AEs to achieve better visual consistency meanwhile maximizing the angle discrepancy of output logits for misclassification.

3 Proposed DifAttack++

3.1 Method Overview

Our proposed DifAttack++ aims to use disentangled VFs and AFs of images to decode AEs in score-based black-box settings, guided by the query feedback from the victim model. As illustrated in Fig. 1, DifAttack++ unfolds in two phases. In the first **training stage**, we

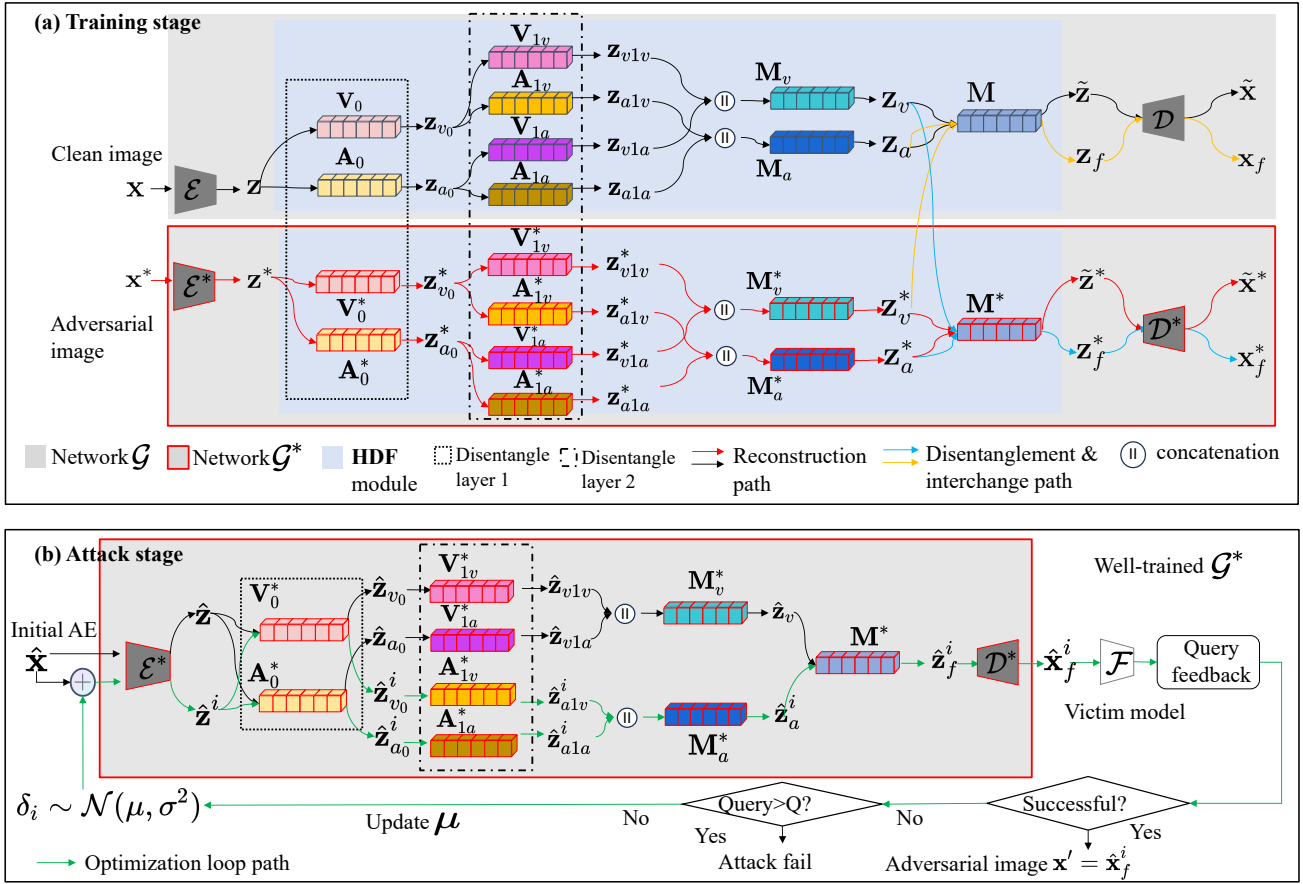


Fig. 1: (a) The training procedure of autoencoders \mathcal{G} and \mathcal{G}^* equipped with our proposed HDF module for disentangling adversarial and visual features. (b) The proposed black-box adversarial attack method, i.e. DifAttack++, incorporated with the pre-trained \mathcal{G}^* .

train two autoencoders \mathcal{G} and \mathcal{G}^* with the same model architecture but different weights. These two models both are able to conduct feature disentanglement and image reconstruction. The training images of \mathcal{G} and \mathcal{G}^* are a set of clean image \mathbf{x} and its AE \mathbf{x}^* , respectively, where \mathbf{x}^* is generated by performing untargeted white-box attacks on surrogate models. Taking \mathbf{x} as an example, \mathcal{G} can disentangle the latent feature \mathbf{z} of \mathbf{x} into the AF \mathbf{z}_a and VF \mathbf{z}_v via our proposed HDF module, and then reconstructs another image $\tilde{\mathbf{x}}$ similar to \mathbf{x} by decoding the fused \mathbf{z}_a and \mathbf{z}_v . \mathcal{G}^* also has such a same functionality for its input. In the second **attack stage**, we leverage the pre-trained \mathcal{G} and \mathcal{G}^* to generate an AE \mathbf{x}' of \mathbf{x} to attack the black-box model \mathcal{F} . This \mathbf{x}' is obtained through an iterative optimization process, wherein we continuously sample a batch of perturbed images to extract AFs $\hat{\mathbf{z}}_a^i$ by updating the sampling parameters according to the query feedback, while keeping the VF $\hat{\mathbf{z}}_v$ consistent with that of the initial image, resulting in batches of reconstructed images $\hat{\mathbf{x}}_f^i$ to query

\mathcal{F} , until either the query number reaches its maximum threshold Q or one of the perturbed images $\hat{\mathbf{x}}_f^i$ successfully deceives \mathcal{F} , thereby yielding the AE $\mathbf{x}' = \hat{\mathbf{x}}_f^i$. For clarity, a summary of notations frequently used in the following sections is provided in Table 1.

3.2 Training Stage: Train Autoencoders \mathcal{G} and \mathcal{G}^*

Suppose that there is a clean image \mathbf{x} in the training dataset and we have pre-trained several white-box surrogate models on this dataset, forming a set \mathcal{C} . Note that the availability of these white-box surrogate models has also been assumed in the existing approaches Lord et al (2022); Feng et al (2022). We adopt the white-box attack method PGD Madry et al (2018) to generate an AE \mathbf{x}^* of \mathbf{x} against a surrogate model \mathcal{C}_j selected randomly from \mathcal{C} . PGD can be replaced by other white-box attack methods or a collection of them. The chosen of white-box attack methods has little impact on the final black-box attack performance, of which the

Table 1: Notations

Sign	Descriptions
\mathcal{F}	Victim/target model
\mathcal{G}	Autoencoder trained on clean images
\mathcal{G}^*	Autoencoder trained on AEs
\mathbf{V}_0	1 st layer for extracting preliminary VFs
\mathbf{A}_0	1 st layer for extracting preliminary AFs
\mathbf{V}_{1v}	2 nd layer for extracting VFs from preliminary VFs
\mathbf{V}_{1a}	2 nd layer for extracting VFs from preliminary AFs
\mathbf{A}_{1v}	2 nd layer for extracting AFs from preliminary VFs
\mathbf{A}_{1a}	2 nd layer for extracting AFs from preliminary AFs
\mathbf{M}_v	fusion layer for obtaining final VFs
\mathbf{M}_a	fusion layer for obtaining final AFs
\mathbf{M}	fusion layer for obtaining latent features
\mathbf{x}	\mathbb{R}^d , clean image
\mathbf{x}^*	\mathbb{R}^d , AE of \mathbf{x} crafted by white-box attacks
\mathbf{x}'	\mathbb{R}^d , AE of \mathbf{x} crafted by black-box attacks
$\tilde{\mathbf{x}}$	\mathbb{R}^d , initial image in the attack stage
$\tilde{\mathbf{z}}$	\mathbb{R}^d , reconstructed image of \mathbf{x}
\mathbf{z}	$\{\mathbb{R}^{d_1}, \dots, \mathbb{R}^{d_k}\}$, latent features of \mathbf{x}
\mathbf{z}_v	$\{\mathbb{R}^{d_1}, \dots, \mathbb{R}^{d_k}\}$, final VFs of \mathbf{x}
\mathbf{z}_a	$\{\mathbb{R}^{d_1}, \dots, \mathbb{R}^{d_k}\}$, final AFs of \mathbf{x}

¹ Other unmentioned symbols with * mean that they are associated with AEs.

comparison experiments has been presented in the supplementary file of DifAttack [Liu et al \(2024a\)](#). Different from our previous work DifAttack which shares one autoencoder \mathcal{G} for both clean and adversarial images, in this work, we assign distinct autoencoders \mathcal{G} and \mathcal{G}^* for the clean and adversarial domain for better training efficiency and black-box attack performance (as empirically verified in the experimental section), since regular AEs usually lie off the manifold of normal images [Lin et al \(2020\)](#). Next, we delve into the details of the disentanglement and reconstruction tasks.

3.2.1 Disentanglement.

For discovering an image’s AF to which the image’s adversarial capability is sensitive, meanwhile ensuring that alterations in this feature maintain minimal impact on the image’s visual appearance, we disentangle AFs and VFs from images’ latent feature. For realizing such a disentanglement, we exchange the AFs and VFs between a pair of clean image and its AE, expecting images reconstructed from these exchanged features to exhibit different adversarial capabilities and visual appearance according to the original images their features stem from.

HDF Module. Specifically, for implementing the feature disentanglement, as illustrated in Fig. 1(a), we design a HDF module, which inputs an image’s latent feature and disentangles this feature into VFs and AFs, finally outputting this image’s reconstructed latent feature via fusing the VFs and AFs. The HDF module

consists of three kinds of convolution layers, including visual layers (\mathbf{V}_0 , \mathbf{V}_{1v} and \mathbf{V}_{1a}), adversarial layers (\mathbf{A}_0 , \mathbf{A}_{1v} and \mathbf{A}_{1a}), and fusion layers (\mathbf{M}_a , \mathbf{M}_v and \mathbf{M}), which are all realized with a series of stacked 1×1 convolution layers. Taking the clean image \mathbf{x} as an example, HDF feeds its latent feature $\mathbf{z} = \mathcal{E}(\mathbf{x})$, where \mathcal{E} denotes a Convolutional Neural Network (CNN)-based encoder, into the **first disentanglement** layer \mathbf{V}_0 and \mathbf{A}_0 , obtaining preliminary VFs \mathbf{z}_{v0} and AFs \mathbf{z}_{a0} respectively as:

$$\begin{aligned}\mathbf{z}_{v0} &= \mathbf{V}_0(\mathbf{z}), \\ \mathbf{z}_{a0} &= \mathbf{A}_0(\mathbf{z}).\end{aligned}\tag{1}$$

Considering that preliminary features \mathbf{z}_{v0} and \mathbf{z}_{a0} obtained from disentanglement layers at one level may still be coupled, we propose to hierarchically append the **second disentanglement** layers \mathbf{V}_{1v} , \mathbf{V}_{1a} , \mathbf{A}_{1v} , and \mathbf{A}_{1a} to preliminary features for achieving finer disentanglement. These four layers are used for extracting the VFs (\mathbf{z}_{v1v}) from the preliminary VFs (\mathbf{z}_{v0}) and VFs (\mathbf{z}_{v1a}) from the preliminary AFs (\mathbf{z}_{a0}), AFs (\mathbf{z}_{a1v}) from the preliminary VFs (\mathbf{z}_{v0}), and AFs (\mathbf{z}_{a1a}) from the preliminary AFs (\mathbf{z}_{a0}) as follows:

$$\begin{aligned}\mathbf{z}_{v1v} &= \mathbf{V}_{1v}(\mathbf{z}_{v0}), \\ \mathbf{z}_{v1a} &= \mathbf{V}_{1a}(\mathbf{z}_{a0}), \\ \mathbf{z}_{a1v} &= \mathbf{A}_{1v}(\mathbf{z}_{v0}), \\ \mathbf{z}_{a1a} &= \mathbf{A}_{1a}(\mathbf{z}_{a0}).\end{aligned}\tag{2}$$

Then we adopt a **visual fusion** layer \mathbf{M}_v to combine these two hierarchically calibrated VFs \mathbf{z}_{v1v} and \mathbf{z}_{v1a} , leading to the final VFs \mathbf{z}_v of the input \mathbf{x} . Similarly, an **adversarial fusion** layer \mathbf{M}_a is employed to obtain the final AFs \mathbf{z}_a from \mathbf{z}_{a1v} and \mathbf{z}_{a1a} . The generation of an image’s final VFs and AFs can be formulated as:

$$\begin{aligned}\mathbf{z}_v &= \mathbf{M}_v(\mathbf{z}_{v1v} || \mathbf{z}_{v1a}), \\ \mathbf{z}_a &= \mathbf{M}_a(\mathbf{z}_{a1v} || \mathbf{z}_{a1a}).\end{aligned}\tag{3}$$

Here, $||$ denotes the channel-wise concatenation. Afterwards, \mathbf{z}_v and \mathbf{z}_a are incorporated into a reconstructed latent feature $\tilde{\mathbf{z}}$ of \mathbf{z} via the fusion layer \mathbf{M} . Overall, we summarize the feature processing operations of HDF module as:

$$\mathcal{HDF}(\mathbf{z}, \mathbf{z}) = \tilde{\mathbf{z}} = \mathbf{M}(\mathbf{z}_v || \mathbf{z}_a).\tag{4}$$

Notably, HDF does not satisfy the commutative property, i.e. $\mathcal{HDF}(\mathbf{z}^*, \mathbf{z}) \neq \mathcal{HDF}(\mathbf{z}, \mathbf{z}^*)$, where $\mathbf{z}^* = \mathcal{E}^*(\mathbf{x}^*)$, unless $\mathbf{z} = \mathbf{z}^*$. To differentiate, we use $\mathcal{HDF}(\cdot)$ and $\mathcal{HDF}^*(\cdot)$ to represent HDF modules in networks \mathcal{G} and \mathcal{G}^* , respectively. It is also easy to extend the process of $\mathcal{HDF}^*(\cdot)$ with an input latent feature \mathbf{z}^* of an AE \mathbf{x}^* as:

$$\mathcal{HDF}^*(\mathbf{z}^*, \mathbf{z}^*) = \tilde{\mathbf{z}}^* = \mathbf{M}^*(\mathbf{z}_v^* || \mathbf{z}_a^*),\tag{5}$$

where $\tilde{\mathbf{z}}^*$ denoted the reconstructed \mathbf{z}^* and \mathbf{M}^* is the fusion layer in \mathcal{G}^* . The final VFs \mathbf{z}_v^* and AFs \mathbf{z}_a^* of \mathbf{x}^* are obtained through the same process as in E.q. (1)-(3), with the only difference being the substitution of modules of \mathcal{G} with modules of \mathcal{G}^* .

Feature Interchange. After elucidating the HDF module, we will now introduce how to utilize HDF to conduct feature interchange for accomplishing disentanglement. Specifically, as depicted by the yellow path in Fig. 1(a), the AF of the clean sample, i.e. \mathbf{z}_a , is firstly concatenated with the VF of the adversarial image, i.e. \mathbf{z}_v^* . Afterward, they are inputted into the fusion layer \mathbf{M} to obtain the fused feature \mathbf{z}_f . Symmetrically, as shown by the blue path, we can obtain another fused feature \mathbf{z}_f^* . These two steps are represented as:

$$\begin{aligned}\mathbf{z}_f &= \mathbf{M}(\mathbf{z}_v^* || \mathbf{z}_a), \\ \mathbf{z}_f^* &= \mathbf{M}^*(\mathbf{z}_v || \mathbf{z}_a^*).\end{aligned}\quad (6)$$

With these two features in hand, we can naturally reconstruct images \mathbf{x}_f and \mathbf{x}_f^* by:

$$\begin{aligned}\mathbf{x}_f &= \mathcal{D}(\mathbf{z}_f), \\ \mathbf{x}_f^* &= \mathcal{D}^*(\mathbf{z}_f^*).\end{aligned}\quad (7)$$

Here, \mathcal{D} and \mathcal{D}^* denote the CNN-based decoder in \mathcal{G} and \mathcal{G}^* , respectively.

Disentanglement Loss. Subsequently, since we desire the AF to control the adversarial capability of the image, while the VF to govern its visual perception, \mathbf{x}_f should be closer to the visual perception of the AE \mathbf{x}^* and be non-adversarial. Conversely, \mathbf{x}_f^* is expected to be closer to the visual perception of the clean image \mathbf{x} and be adversarial against all surrogate models so as to improve the generalization ability of the AF on different classifiers. Hence, we aim to minimize the disentanglement loss L_{dis} that is defined as:

$$\begin{aligned}L_{dis} &= \|\mathbf{x}^* - \mathbf{x}_f\|_2 + \frac{1}{N} \sum_{j=1}^N L_{adv}(\mathbf{x}_f, y, 1, \mathcal{C}_j, k) \\ &+ \|\mathbf{x} - \mathbf{x}_f^*\|_2 + \frac{1}{N} \sum_{j=1}^N L_{adv}(\mathbf{x}_f^*, y, 0, \mathcal{C}_j, k),\end{aligned}\quad (8)$$

where N signifies the cardinality of the surrogate model set \mathbb{C} . The l_2 norm measures the Euclidean distance of two images, and L_{adv} is employed to evaluate the adversarial ability, whose definition Carlini and Wagner (2017) is:

$$\begin{aligned}L_{adv}(\mathbf{x}, y, v, \mathcal{C}_j, k) &= \\ \max \left\{ \mathbb{I}(v) \cdot (\mathcal{C}_j(\mathbf{x}, y) - \max_{d \neq y} \mathcal{C}_j(\mathbf{x}, d)), -k \right\}.\end{aligned}\quad (9)$$

The value of v can be set as 0 or 1. $\mathbb{I}(0) = 1$ means an untargeted attack with a ground-truth label of y , while $\mathbb{I}(1) = -1$ indicates a targeted attack with a target

Algorithm 1 The proposed DifAttack++ method.

Input: target classifier \mathcal{F} ; autoencoder \mathcal{G}^* pretrained in the adversarial domain; clean image \mathbf{x} ; initial image $\hat{\mathbf{x}}$; max query budget $Q > 0$; distortion budget ϵ ; ground-truth/target label y for untargeted/targeted attacks; learning rate η ; variance σ ; v, k in Eq.(18); sample scale τ .

Output: Adversarial image \mathbf{x}' .

```

1: Let  $q \leftarrow 0, \mathbf{x}' \leftarrow \hat{\mathbf{x}}, \mu \sim \mathcal{N}(0, I)$ 
2: while  $q + \tau \leq Q$  do
3:    $\gamma_1, \dots, \gamma_i, \dots, \gamma_\tau \sim \mathcal{N}(0, I)$ 
4:    $\delta_i \leftarrow \mu + \sigma \gamma_i, \forall i \in \{1, \dots, \tau\}$ 
5:   if In close-set scenarios then
6:     Obtaining  $\hat{\mathbf{x}}_f^i$  using E.q. (15), (13), (16), and (17).
7:   else if In open-set scenarios then
8:     Obtaining  $\hat{\mathbf{x}}_f^i$  using E.q. (21), (22), (16), and (17).
9:   end if
10:   $l_i \leftarrow L_{adv}(\hat{\mathbf{x}}_f^i, y, v, \mathcal{F}, k), \forall i$ 
11:   $q \leftarrow q + \tau$ 
12:  if  $\exists l_i = -k$  then
13:     $\mathbf{x}' \leftarrow \hat{\mathbf{x}}_f^i$ 
14:    break
15:  else
16:     $\hat{l}_i \leftarrow (l_i - \text{mean}(\{l_i\})) / \text{std}(\{l_i\}), \forall i$ 
17:     $\mu \leftarrow \mu - \frac{\eta}{\tau \sigma} \sum_{i=1}^{\tau} \hat{l}_i \gamma_i$ 
18:  end if
19: end while
20: return  $\mathbf{x}'$ 
```

category of y . $\mathcal{C}_j(\mathbf{x}, d)$ is the output score of \mathcal{C}_j at the d -th class. The adjustable constant $k > 0$ controls the adversarial extent.

3.2.2 Reconstruction.

For achieving a cycle consistency Zhu et al (2017) with regard to feature disentanglement, as depicted in the reconstruction paths of Fig. 1(a), the autoencoder is expected to reconstruct an input image well even when its latent feature is processed by the HDF module. Therefore, the output of HDF modules, i.e. $\tilde{\mathbf{z}}$ and $\tilde{\mathbf{z}}^*$, are expected to reconstruct $\tilde{\mathbf{x}} \approx \mathbf{x}$ and $\tilde{\mathbf{x}}^* \approx \mathbf{x}^*$ through:

$$\begin{aligned}\tilde{\mathbf{x}} &= \mathcal{D}(\mathcal{HDF}(\mathbf{z}, \mathbf{z})), \\ \tilde{\mathbf{x}}^* &= \mathcal{D}^*(\mathcal{HDF}^*(\mathbf{z}^*, \mathbf{z}^*)).\end{aligned}\quad (10)$$

Consequently, we define the reconstruction loss L_{rec} of \mathcal{G} and \mathcal{G}^* by:

$$L_{rec} = \|\mathbf{x} - \tilde{\mathbf{x}}\|_2 + \|\mathbf{x}^* - \tilde{\mathbf{x}}^*\|_2. \quad (11)$$

Eventually, the loss function to be minimized during training networks \mathcal{G} and \mathcal{G}^* can be computed as:

$$L_{all} = \lambda \cdot L_{rec} + L_{dis}, \quad (12)$$

where the hyper-parameter λ balances two loss terms.

3.3 Attack Stage: Generate the AE \mathbf{x}'

Upon obtaining the well-trained \mathcal{G} and \mathcal{G}^* , in the subsequent attack stage, we can utilize them to generate AEs in a black-box setting. As shown in Fig. 1(b), to perform a black-box attack against the victim model \mathcal{F} with a clean image \mathbf{x} , we maintain the VF for decoding the perturbed image $\hat{\mathbf{x}}_f$ to be identical to that of the initial image $\hat{\mathbf{x}}$, i.e. $\hat{\mathbf{z}}_v$ that is obtained by:

$$\begin{aligned}\hat{\mathbf{z}} &= \mathcal{E}^*(\hat{\mathbf{x}}), \\ \hat{\mathbf{z}}_{v0} &= \mathbf{V}_0^*(\hat{\mathbf{z}}), \\ \hat{\mathbf{z}}_{a0} &= \mathbf{A}_0^*(\hat{\mathbf{z}}), \\ \hat{\mathbf{z}}_{v1v} &= \mathbf{V}_{1v}^*(\hat{\mathbf{z}}_{v0}), \\ \hat{\mathbf{z}}_{v1a} &= \mathbf{V}_{1a}^*(\hat{\mathbf{z}}_{a0}), \\ \hat{\mathbf{z}}_v &= \mathbf{M}_v^*(\hat{\mathbf{z}}_{v1v} || \hat{\mathbf{z}}_{v1a}).\end{aligned}\quad (13)$$

This makes $\hat{\mathbf{x}}_f$ remain in close proximity to the clean image as much as possible. Meanwhile, our objective is to identify an AF $\hat{\mathbf{z}}_a$ that, when combined with $\hat{\mathbf{z}}_v$, has the ability to deceive \mathcal{F} . For example, in untargeted attacks, our attack objective targets at finding an image $\hat{\mathbf{x}}_f$ by:

$$\begin{aligned}\hat{\mathbf{x}}_f &= \mathcal{D}^*(\mathbf{M}^*(\hat{\mathbf{z}}_v || \hat{\mathbf{z}}_a)), \\ s.t. \arg \max_d \mathcal{F}(\hat{\mathbf{x}}_f, d) &\neq y \text{ and } ||\hat{\mathbf{x}}_f - \mathbf{x}||_p \leq \epsilon.\end{aligned}\quad (14)$$

Here y denotes the ground-truth label of \mathbf{x} . In targeted attacks, the first constraint is transformed to $\arg \max_d \mathcal{F}(\hat{\mathbf{x}}_f, d) = y$ with y being the target class. Note that in E.q. (13) and (14) we use modules of \mathcal{G}^* rather than \mathcal{G} , and the reason will be clarified later.

For seeking out such a $\hat{\mathbf{z}}_a$ to meet E.q. (14), firstly, we have to determine the initial image $\hat{\mathbf{x}}$ for the attack stage so as to acquire $\hat{\mathbf{z}}_v$ like in E.q. (13). Considering the adversarial transferability across different models, we leverage an AE rather than the clean image to initialize a more aggressive AF, expecting to enhance attack efficiency. This initialization strategy is feasible with known class information and available surrogate models in closed-set scenarios, since we can directly generate a transferable AE through a white-box attack method against surrogate models to serve as the initial image. Conversely, in open-set scenarios, due to the uncertainty of class categories, a clean image is more suitable for initializing the attack, i.e. $\hat{\mathbf{x}} = \mathbf{x}$. We will next elaborate on the attack processes separately for both closed-set and open-set scenarios.

In **closed-set** scenarios, as illustrated in Fig. 1(b), we firstly generate a transferable AE $\hat{\mathbf{x}}$ of \mathbf{x} against an ensemble of local surrogate models using a transferable white-box attack \mathcal{A} . In this work, we choose SI-NI-TI-DIM Lin et al (2019) as \mathcal{A} , which is one of the most

powerful transferable methods. \mathcal{A} could be replaced as other attack methods with stronger transferability in the future. Formally, the generation of the initial image at the untargeted attack stage is expressed as:

$$\begin{aligned}\hat{\mathbf{x}} &= \mathcal{A}(\mathbb{C}, \mathbf{x}), \\ s.t. \arg \max_d \mathcal{C}_j(\hat{\mathbf{x}}, d) &\neq y \text{ and } ||\hat{\mathbf{x}} - \mathbf{x}||_p \leq \epsilon, \forall \mathcal{C}_j \in \mathbb{C}.\end{aligned}\quad (15)$$

For targeted black-box attacks, this formulation only needs to replace the constraint $\arg \max_d \mathcal{C}_j(\hat{\mathbf{x}}, d) \neq y$ where y represents the ground-truth label with $\arg \max_d \mathcal{C}_j(\hat{\mathbf{x}}, d) = y$ where y denotes the target label. Then we can combine E.q. (15) and (13) to acquire $\hat{\mathbf{z}}_v$, and maintain the VF for decoding the perturbed candidate image $\hat{\mathbf{x}}_f$ to be identical to the VF of $\hat{\mathbf{x}}$, i.e. $\hat{\mathbf{z}}_v$. Note that $\hat{\mathbf{z}}_v$ in E.q. (13) is disentangled by \mathcal{G}^* but not \mathcal{G} since $\hat{\mathbf{x}}$ belongs to the adversarial domain. Nextly, we have to identify proper AFs $\hat{\mathbf{z}}_a$ that, when fused with $\hat{\mathbf{z}}_v$, has the ability to deceive \mathcal{F} . Therefore, we aim to discover a perturbation δ whose corresponding perturbed image $\hat{\mathbf{x}} + \delta$ can be used to extract such AFs. Formally, we obtain $\hat{\mathbf{z}}_a$ via:

$$\begin{aligned}\hat{\mathbf{z}} &= \mathcal{E}^*(\hat{\mathbf{x}} + \delta), \\ \hat{\mathbf{z}}_{v0} &= \mathbf{V}_0^*(\hat{\mathbf{z}}), \\ \hat{\mathbf{z}}_{a0} &= \mathbf{A}_0^*(\hat{\mathbf{z}}), \\ \hat{\mathbf{z}}_{a1v} &= \mathbf{A}_{1v}^*(\hat{\mathbf{z}}_{v0}), \\ \hat{\mathbf{z}}_{a1a} &= \mathbf{A}_{1a}^*(\hat{\mathbf{z}}_{a0}), \\ \hat{\mathbf{z}}_a &= \mathbf{M}_a^*(\hat{\mathbf{z}}_{a1v} || \hat{\mathbf{z}}_{a1a}).\end{aligned}\quad (16)$$

Then in close-set scenarios, the perturbed AE $\hat{\mathbf{x}}_f$ can be reconstructed as follows:

$$\hat{\mathbf{x}}_f = \Pi_{\epsilon, \mathbf{x}} \left(\mathcal{D}^* \left(\mathbf{M}^*(\hat{\mathbf{z}}_v || \hat{\mathbf{z}}_a) \right) \right). \quad (17)$$

where $\hat{\mathbf{z}}_v$ is obtained by E.q. (13) and keep invariant while $\hat{\mathbf{z}}_a$ is iteratively optimized by using E.q. (16) and continuously updated δ . The operation $\Pi_{\epsilon, \mathbf{x}}$ represents the projection of the input image into the l_p ball bounded by ϵ and centered at \mathbf{x} . This forces the adversarial perturbation to remain within the specified constraint. For simplicity, we recast the right-hand side of Eq.(17) as $\mathbf{T}(\hat{\mathbf{x}} + \delta)$. To find an adversarial $\hat{\mathbf{x}}_f$, by combining Eq.(17) and using the transformation of variable approach, we formulate our attack objective in E.q. (14) in a unified manner as:

$$\begin{aligned}\min_{\mu} \mathbb{E}_{\mathcal{N}(\delta | \mu, \sigma^2)} L_{adv}(\mathbf{T}(\hat{\mathbf{x}} + \delta), y, v, \mathcal{F}, k), \\ s.t. ||\mathbf{T}(\hat{\mathbf{x}} + \delta) - \mathbf{x}|| \leq \epsilon,\end{aligned}\quad (18)$$

where $\hat{\mathbf{x}}_f = \mathbf{T}(\hat{\mathbf{x}} + \delta)$ satisfies $\arg \max_d \mathcal{F}(\hat{\mathbf{x}}_f, d) \neq y$ for untargeted attacks with y representing the ground truth label of \mathbf{x} or $\arg \max_d \mathcal{F}(\hat{\mathbf{x}}_f, d) = y$ for targeted

attacks with y denoting the target class. We sample δ from a Gaussian distribution $\mathcal{N}(\mu, \sigma^2)$ where the mean μ is to be optimized and the variance σ is fixed to be the optimal value through performing a grid search. For optimizing μ , we adopt the natural evolution strategies method to estimate the gradient of the expectation of L_{adv} in Eq.(18) w.r.t μ . When using stochastic gradient descent with a learning rate η and a batch size τ , the update rule for μ is as follows:

$$\mu \leftarrow \mu - \frac{\eta}{\tau\sigma} \sum_{i=1}^{\tau} \gamma_i L_{adv}(\mathbf{T}(\hat{\mathbf{x}} + \mu + \sigma\gamma_i), y, v, \mathcal{F}, k). \quad (19)$$

Here, $\gamma_i \sim \mathcal{N}(0, I)$, and by setting $\delta_i = \mu + \sigma\gamma_i$, we obtain $\delta_i \sim \mathcal{N}(\mu, \sigma^2)$.

By obtaining a solution μ to E.q. (18) using E.q. (19), we simultaneously achieve the ultimate successful AE \mathbf{x}' by calculating:

$$\mathbf{x}' = \hat{\mathbf{x}}_f^i = \mathbf{T}(\hat{\mathbf{x}} + \mu + \sigma\gamma_i). \quad (20)$$

In **open-set** scenarios, due to the uncertainty of images' categories, surrogate models are highly likely to predict outputs inconsistent with that of victim models and consequently generate AEs with weak transferabilities or even with side effects. Thus we set the clean image \mathbf{x} as the initial image $\hat{\mathbf{x}}$, i.e.

$$\hat{\mathbf{x}} = \mathbf{x}, \quad (21)$$

and disentangle VFs of $\hat{\mathbf{x}}$ via \mathcal{G} that belongs to the clean domain as:

$$\begin{aligned} \hat{\mathbf{z}} &= \mathcal{E}(\hat{\mathbf{x}}), \\ \hat{\mathbf{z}}_{v0} &= \mathbf{V}_0(\hat{\mathbf{z}}), \\ \hat{\mathbf{z}}_{a0} &= \mathbf{A}_0(\hat{\mathbf{z}}), \\ \hat{\mathbf{z}}_{v1v} &= \mathbf{V}_{1v}(\hat{\mathbf{z}}_{v0}), \\ \hat{\mathbf{z}}_{v1a} &= \mathbf{V}_{1a}(\hat{\mathbf{z}}_{a0}), \\ \hat{\mathbf{z}}_v &= \mathbf{M}_v(\hat{\mathbf{z}}_{v1v} || \hat{\mathbf{z}}_{v1a}). \end{aligned} \quad (22)$$

Meanwhile, we still extract AFs $\hat{\mathbf{z}}_a$ of the perturbed image $\hat{\mathbf{x}} + \delta$ with \mathcal{G}^* as E.q. (16) to keep fused \mathbf{x}' lie on the adversarial domain as much as possible. Similar to close-set scenarios, it is easy to obtain the perturbed image $\hat{\mathbf{x}}_f$ in open-set scenarios as in E.q. (17), but obtaining $\hat{\mathbf{z}}_v$ in E.q. (17) using E.q. (21) and (22) sequentially, and $\hat{\mathbf{z}}_a$ calculated by E.q. (16). Then we can use the same solution as in the closed set scenario mentioned above to obtain a successful AE \mathbf{x}' .

Overall, our DifAttack++ is summarized in Algorithm 1. Note that, in line 16, we normalize the L_{adv} of each perturbed image to stabilize convergence by taking inspiration from the \mathcal{N} Attack Li et al (2019) method.



Fig. 2: The visualization of AEs produced by MCGSquare Andriushchenko et al (2020) and DifAttack++ (Ours).

4 Experiments

In this section, we compare our DifAttack++ with SOTA score-based black-box attack methods in both close-set and open-set scenarios. Ablation experiments on the cross domain, the HDF module, and the chosen of initial image in the attack stage are also conducted.

4.1 Experiment Setup

4.1.1 Datasets.

We mainly conduct experiments on the large-scale ImageNet-1k (abbreviated as ImageNet) Deng et al (2009) dataset in close-set scenarios, on Food101 Bossard et al (2014) and ObjectNet Barbu et al (2019) in open-set scenarios. Food101 consists of 101 food categories, and ObjectNet contains natural images with controls for rotation, background, and viewpoint, which poses more difficult challenges for object recognitions. Images in ImageNet, Food101 and ObjectNet are cropped and resized to 224×224 , 224×224 and 336×336 for adapting their associated classifiers. When conducting attacks on ObjectNet in open-set scenarios, we exclude 131 classes that overlap with ImageNet, referring to Barbu et al (2019) for more details about these classes.

4.1.2 Classifiers.

For ImageNet, we collect eight pre-trained classifiers with different architectures, i.e. ResNet18, VGG16, GoogleNet, SqueezeNet, ConvNeXtBase, EfficientNet-B3, Swin-V2-T, and ResNet101 provided by torchvision². Their Top-1 classification accuracies on the Im-

² <https://pytorch.org/vision/stable/index.html>

Table 2: The attack success rate (ASR %), average number of queries (Avg.Q) of test images in targeted attacks with the target class 864 or untargeted attacks for ImageNet. The best and second best Avg.Q are **bold** and underlined, respectively.

Victims	GoogleNet				VGG16				ResNet18				SqueezeNet				Average			
Settings	Targeted		Untargeted		Targeted		Untargeted		Targeted		Untargeted		Targeted		Untargeted		Targeted		Untargeted	
Metrics	ASR	Avg.Q	ASR	Avg.Q	ASR	Avg.Q	ASR	Avg.Q	ASR	Avg.Q	ASR	Avg.Q	ASR	Avg.Q	ASR	Avg.Q	ASR	Avg.Q	ASR	Avg.Q
SignH	28.1%	9,021	95.5%	1,504	60.8%	7,606	100.0%	702	49.8%	7,935	<u>99.5%</u>	931	45.7%	8,315	100.0%	363	46.1%	8,219	98.8%	875
NES	37.7%	8,748	100.0%	1,234	47.7%	8,328	98.0%	1,068	54.3%	7,988	<u>97.5%</u>	1,264	45.7%	8,235	91.0%	1,711	46.4%	8,325	96.6%	1,319
\mathcal{N} Attack	76.9%	6,883	100.0%	878	93.5%	5,924	100.0%	752	94.5%	5,324	100.0%	780	90.0%	5,644	100.0%	563	88.7%	5,944	100.0%	743
SimBA	77.5%	5,874	100.0%	865	<u>97.5%</u>	3,505	99.0%	533	97.0%	3,873	<u>99.5%</u>	614	94.0%	4,230	<u>99.5%</u>	428	91.5%	4,371	<u>99.5%</u>	610
BASES	12.5%	8,901	81.7%	2,080	26.7%	8,229	95.5%	564	15.4%	9,228	85.1%	1,717	35.3%	7,179	86.4%	1,549	22.5%	8,384	<u>87.2%</u>	1,478
P-RGF	34.2%	7,790	93.0%	1,162	58.3%	6,093	98.0%	529	51.3%	6,393	96.0%	711	65.3%	5,433	95.0%	796	52.3%	6,427	95.5%	800
Subspace	50.3%	6,642	95.5%	994	68.3%	4,964	95.5%	867	66.3%	4,750	94.5%	917	33.2%	8,063	97.0%	566	54.5%	6,105	95.6%	836
GFCs	60.0%	6,359	<u>96.5%</u>	1,348	93.0%	3,358	100.0%	515	95.0%	3,274	100.0%	739	72.5%	6,127	98.5%	658	80.1%	4,780	98.8%	815
CGA	90.9%	4,645	100.0%	<u>139</u>	91.1%	4,801	<u>99.4%</u>	137	91.6%	4,222	97.3%	475	93.2%	3,972	99.3%	202	91.7%	4,410	99.0%	238
MCGSquare	96.0%	2,937	100.0%	174	100.0%	<u>1,816</u>	100.0%	49	<u>99.5%</u>	<u>1,346</u>	100.0%	61	99.0%	<u>1,633</u>	100.0%	37	98.6%	<u>1,933</u>	100.0%	<u>80</u>
DifAttack	<u>97.0%</u>	3,201	100.0%	165	100.0%	2,246	100.0%	123	100.0%	1,901	100.0%	156	98.0%	2,793	100.0%	90	<u>98.8%</u>	2,535	100.0%	134
DifAttack++	99.5%	1,530	100.0%	80	100.0%	969	100.0%	<u>52</u>	100.0%	957	100.0%	<u>62</u>	99.0%	1,389	100.0%	<u>41</u>	99.6%	1,211	100.0%	58

ageNet test dataset are 69.8%, 73.4%, 69.8%, 58.2%, 84.1%, 82.0%, 82.1%, and 81.9% respectively. These eight classifiers is divided into two groups for experiments. The first group, referred to as the “simple group”, consists of the former four classifiers with relatively lower classification accuracy (below 80%) and relatively simple architectures, which were previously used in our DifAttack work. The second group, denoted as the “complex group”, comprises the subsequent four classifiers not being investigated in DifAttack. These models exhibit higher accuracy (above 80%) and possess diverse and complicated architectures. We select three classifiers from each group as surrogate models, while the remaining one in this group serves as the victim model.

For Food101 and ObjectNet, we use well pretrained OpenAI’s CLIP models provided by Ilharco et al (2021) as victim models to further verify the attack ability of DifAttack++ towards foundation models. They are ViT-B/16 trained on public available image-caption data and ViT-H-14-CLIPA-336 trained on DataComp-1B dataset Gadre et al (2024), which achieve 88.7% and 77.4% zero-shot accuracy on Food101 and ObjectNet, respectively.

4.1.3 Comparative Methods.

We compare our DifAttack++ with SOTA approaches, including DifAttack Liu et al (2024a), MCG Yin et al (2023a), SignH Al-Dujaili and O’Reilly (2020), NES Ilyas et al (2018), \mathcal{N} Attack Li et al (2019), SimBA-DCT (shorted as SimBA) Guo et al (2019a), BASES Cai et al (2022), P-RGF Cheng et al (2019), Subspace Guo et al (2019b), GFCs Lord et al (2022) and CGA Feng et al (2022). We evaluate them according to their official source codes. Due to the absence of pre-trained models and code, the experimental results of the CGA method on ImageNet are cited from its published paper. Since MCG Yin et al (2023a) could be combined with

different kinds of black-box attack, we choose the best query-efficient combination, MCG+SquareAttack An-driushchenko et al (2020), a.k.a MCGSquare, as a representative. The attack performance of MCG integrated with other attack methods lag far behind MCGSquare. Another work Liu et al (2024b) reports remarkable attack performance in their works, but there is unavailable public models or codes.

4.1.4 Parameters.

Following many previous works, we also set the maximum perturbation on ImageNet, Food101 and ObjectNet to 12/255. The maximum query number is all set to 10,000. For the real-world Imaggia API, the maximum query number is limited to 500 due to their query limit. In our DifAttack++, we set $\lambda = 1$, $\sigma = 0.1$, $\eta = 0.01$, $k = 5$ or 0 for Eq.(8) and (19).

4.2 The Close-set Scenario

4.2.1 Black-box Attacks against ImageNet Classifiers.

Table 2 and 3 present the ASR and average query numbers (Avg.Q) when attacking victim models from the “simple group” or “complex group”. For targeted attacks, we randomly select a target class (864) and 1,000 images correctly classified by the victim model, excluding those belonging to the selected class, as the test set. It is demonstrated that on average, our DifAttack++ surpasses all compared methods in both ASR and Avg.Q. Moreover, in both targeted and untargeted attacks, DifAttack++ usually achieves the same or higher ASR than the second-best method, MCGSquare, while using much fewer Avg.Q especially for the challenging targeted attacks and powerful victim models. For example, in the targeted attacks for the “simple

Table 3: The attack success rate (ASR %), average number of queries (Avg.Q) of test images in targeted attacks with the target class 864 or untargeted attacks for ImageNet. The best and second best Avg.Q are **bold** and underlined, respectively.

Victims	Swin-V2-T				EfficientNet-B3				ResNet101				ConvNeXtBase				Avg.			
Settings	Targeted		Untargeted		Targeted		Untargeted		Targeted		Untargeted		Targeted		Untargeted		Targeted		Untargeted	
Metrics	ASR	Avg.Q	ASR	Avg.Q	ASR	Avg.Q	ASR	Avg.Q	ASR	Avg.Q	ASR	Avg.Q	ASR	Avg.Q	ASR	Avg.Q	ASR	Avg.Q	ASR	Avg.Q
SignH	44.2%	8,212	82.9%	3,049	31.7%	8,847	87.4%	2,611	6.5%	9,744	66.3%	4,670	20.6%	9,216	81.9%	3,979	25.8%	9,005	79.6%	3,577
NES	30.7%	8,722	95.0%	2,093	15.6%	9,382	95.5%	2,185	10.6%	9,606	90.0%	3,013	11.1%	9,471	86.4%	3,561	17.0%	9,295	91.7%	2,713
NAttack	66.8%	7,473	99.0%	1,298	32.2%	8,825	99.0%	1,390	20.6%	9,128	96.5%	1,888	40.7%	8,609	100.0%	2,012	40.1%	8,509	98.6%	1,647
SimBA	84.0%	5,822	98.5%	2,185	65.0%	7,585	98.0%	1,419	30.5%	9,579	73.0%	5,314	90.0%	5,328	98.5%	1,885	67.4%	7,078	92.0%	2,701
P-RGF	62.3%	4,610	96.5%	755	49.3%	6,244	90.0%	1,345	34.7%	8,087	89.5%	1,301	57.3%	5,720	88.9%	1,381	50.9%	6,165	91.2%	1,196
Subspace	61.3%	6,597	99.0%	882	55.3%	6,834	95.5%	993	35.7%	7,978	95.5%	1,198	76.9%	5,206	<u>99.0%</u>	569	57.3%	6,654	97.2%	910
GFCs	61.5%	5,683	86.5%	1,794	57.0%	5,897	89.0%	1,692	36.0%	7,577	87.0%	1,521	71.0%	4,270	91.5%	1,621	56.4%	5,857	88.5%	1,657
MCGSquare	99.0%	2,352	100.0%	251	95.0%	3,738	99.5%	463	75.5%	6,079	99.5%	400	100.0%	2,762	100.0%	226	92.4%	3,733	<u>99.8%</u>	335
DifAttack	95.0%	3,962	100.0%	454	62.0%	6,555	99.5%	576	50.0%	7,466	99.0%	675	98.0%	4,625	100.0%	774	76.3%	5,704	99.6%	620
DifAttack++	100.0%	1,520	100.0%	137	<u>90.5%</u>	3,631	100.0%	225	79.5%	4,672	99.5%	264	100.0%	1,627	100.0%	159	92.5%	2,862	100.0%	196

Table 4: The comparison of AE’s visual quality between DifAttack++ and MCGSquare.

Methods	PSNR \uparrow	SSIM \uparrow	LPIPS \downarrow	MSE \downarrow
MCGSquare	24.96	0.7109	0.3154	27.26
DifAttack++	27.51	0.7844	0.2010	22.36

group” (see Table 2), DifAttack++ improves the average ASR by an average of 1% while reducing query counts by 37.4%. For the complex group (see Table 3), DifAttack++ achieves a higher ASR in targeted attacks while reducing the Avg.Q on average by nearly 1,000, and in untargeted attacks, it further decreases the number of queries by 41.5%. Besides the overall attack efficiency improvement, DifAttack++ also significantly outperforms MCGSquare in terms of the visual quality of AEs, which makes DifAttack++ less perceptible and more practical. Now we present more details in the following subsection.

4.2.2 DifAttack++’s Advantages over MCGSquare.

AE’s Qualitative Visual Quality. Due to the algorithm characteristics, SquareAttack results in severe visual distortions (e.g., colored blocks or stripes) in their generated AEs (see more examples in Andriushchenko et al (2020)). So AEs generated by MCGSquare, which enhances the preliminary SquareAttack method by using meta learning and historic query information, inevitably exhibits such severe visual perturbations, as can be seen from Fig. 2. In contrast, our DifAttack++ achieves efficient attacks while ensuring much subtle visual perturbation in the generated AEs, making them imperceptible to human eyes. This is because we effectively disentangle the visual and adversarial features of images, and ensure that the VFs of the image remain almost unchanged during the generation of AEs, while updating only the AFs. **AE’s Quantitative Visual Quality.** We also evaluate the average image quality metrics of a set of AEs generated by our DifAttack++

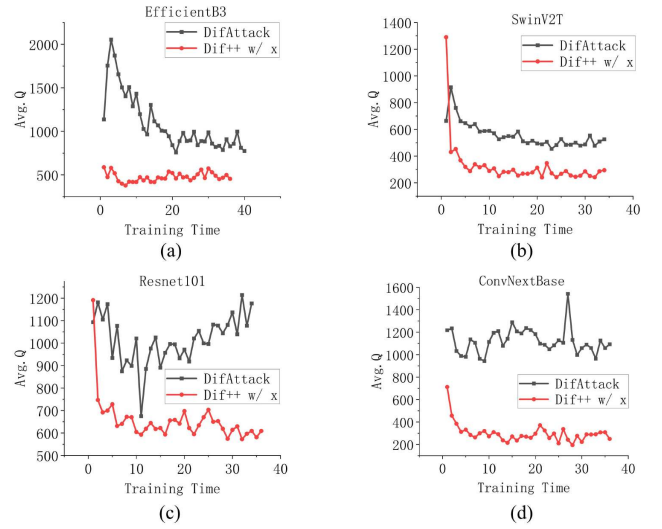


Fig. 3: The comparison of Avg.Q in untargeted attacks on the ImageNet test dataset between DifAttack and DifAttack++ w/ x, in which our DifAttack++ method begins the attack stage with clean images to maintain fairness.

or MCGSquare, when comparing these AEs with their associated clean images. These AEs are randomly produced from the ImageNet test dataset and successfully fool the ResNet18 model. From the result summarized in Table 4 we can see that in terms of the four metrics considered, the quality of AEs’ generated by DifAttack++ significantly surpasses that of MCGSquare, e.g. over 2.5 higher PSNR values.

4.2.3 DifAttack++’s Advantages over DifAttack.

From Table 2-3, it is demonstrated that our DifAttack++ outperforms DifAttack significantly in terms of ASR and query efficiency. Specifically, when attacking relatively simple victim models, as shown in Table 2, DifAttack++ boosts the Avg.Q of DifAttack by

Table 5: The ASR and Avg.Q in untargeted attacks against CLIP models.

Datasets→	Food101		ObjectNet	
Methods↓	ASR	Avg.Q	ASR	Avg.Q
SimBA	100.0%	157	86.5%	2,636
SignH	96.0%	1,139	90.0%	2,073
\mathcal{N} Attack	100.0%	342	100.0%	554
NES	100.0%	614	96.5%	1,665
DifAttack	100.0%	132	100.0%	239
DifAttack++	100.0%	84	100.0%	213

56.7% and 26.2% in average in untargeted and targeted attacks, respectively. When the complexity of victim models increases (see Table 3), the gains of DifAttack++ are even more pronounced, with 68.4% and 35.9% enhancements in Avg.Q, meanwhile obtaining 13.8% higher ASR in targeted attacks. In this subsection, we illustrate that DifAttack++ also greatly enhances the training efficiency and test stability. In Fig. 3, we depict the changes of Avg.Q under untargeted attacks by DifAttack++ or DifAttack, where attacks are conducted on the same ImageNet test set and four different victim models over training time. It is worth mentioning that, for fair comparison, in this close-set scenario, we use the results of DifAttack++ with clean images as the initial image for the attack stage, denoted as DifAttack++ w/ \mathbf{x} , to align with DifAttack. As shown in Fig. 3(a) and (b), it is indicated that, generally, models trained with DifAttack++ converge faster. Additionally, DifAttack++ is less prone to overfitting compared to DifAttack, where overfitting leads to a gradual increase in Avg.Q, as depicted in Fig. 3(c). Furthermore, DifAttack++ demonstrates more stable performance on the test set with smaller oscillations, as illustrated in Fig. 3(c) and (d).

4.3 The Open-set Scenario

The experiments above confirms that in closed-set scenarios, DifAttack++ achieves superior ASR and query efficiency compared to compared SOTA methods while maintaining high visual quality of AEs. In this subsection, we will further evaluate attack performance in open-set scenarios, where the victim model’s training set differs from that of surrogate models. We use the challenging task of attacking CLIP models trained on large-scale datasets and a real-world API with unknown training data as examples.

4.3.1 Black-box Attacks against CLIP models.

Take the untargeted attack as an example, we generate AEs for test images from food101 and objectNet

Table 6: The ASR and Avg.Q when attacking Imagga API.

Settings→	Untargeted		Targeted	
Methods↓	ASR	Avg.Q	ASR	Avg.Q
SignH	70.0	186.3	63.6	211.8
Nattack	76.7	192.1	38.2	406.1
SimBA	60.0	291.6	54.5	244.0
GFCS	70.0	198.3	-	-
MCGSquare	73.3	134.1	-	-
DifAttack	80.0	132.2	68.2	196.8
DifAttack++	86.7	92.1	72.7	163.4

datasets to attack their corresponding CLIP models. The surrogate models are Swin-V2-T, ConvNeXtBase, and ResNet101 pretrained on ImageNet. As shown in Table 5, it is worth noting that we only evaluate attack methods applicable for such an open-set scenario. The results demonstrate that DifAttack++ achieves significant improvements in ASR and Avg.Q over other black-box methods, especially when the victim model and classification task are challenging, e.g. classification on ObjectNet via ViT-H-14-CLIPA-336 model. Both the methods based on feature disentanglement, DifAttack and DifAttack++ perform satisfactorily, with DifAttack++ showing further improvements in query efficiency over DifAttack.

4.3.2 Black-box Attacks against Real-world API.

To evaluate the attack performance in a more practical open-set scenario, we assess comparative methods by attacking the real-world Imagga API [Imagga \(2024\)](#). This API utilizes a recognition model trained on a diverse dataset of daily images spanning over 3,000 unknown categories. The Imagga provides multiple predicted classes and corresponding scores for each query image. Due to the API’s call limits, we choose the top-performing six methods in the above experiments as the comparative methods, which are DifAttack, MCGSquare, CGA, GFCS, SimBA, \mathcal{N} Attack and SignH. We use the autoencoder and surrogate models pre-trained on ImageNet to extract disentangled features of test images from ImageNet. In untargeted attacks, we aim to remove top 3 predicted classes of clean images. In targeted attacks, we set the target class to be the 2nd-highest scoring class among API’s predicted classes. The experimental results in Table 6 indicate that even when the actual training dataset is completely unknown, our DifAttack++ still exhibits superior ASR and Avg.Q simultaneously than comparative methods both in untargeted and targeted attacks. Notably, GFCS and MCGSquare successfully generate AEs in untargeted attacks but not in targeted attacks,

Table 7: The ASR of AEs from ImageNet against various SOTA defensive techniques in the untargeted setting.

Methods	AT	BitRed	NRP	DiffPure	Avg.ASR
SignH	36.7	38.0	28.9	12.6	29.1
NES	18.6	21.0	31.3	20.0	22.7
\mathcal{N} Attack	39.2	45.0	34.9	24.0	35.8
SimBA	39.5	14.5	25.8	13.1	23.2
BASES	0.0	58.5	28.5	8.6	23.9
P-RGF	43.2	38.0	37.5	30.4	37.3
Subspace	54.8	54.0	29.5	14.8	38.3
GFCS	6.8	21.5	32.9	22.5	20.9
MCGSquare	70.5	72.0	10.0	65.5	49.2
DifAttack	52.5	46.5	41.5	28.5	42.3
DifAttack++	66.0	77.5	48.0	48.0	57.8

since they are unable to craft AEs when the target class does not occur in the output of surrogate models. It is worth noting that due to the possibility of continuous model updates of real-world APIs over time, we retest the comparative methods, which makes the experimental results inconsistent with those in DifAttack.

4.4 Black-box Attack against Defensive Methods

It is also important to evaluate the performance of attack methods against defensive strategies. We compare the ASR of comparative methods in untargeted attacks when encountering several SOTA defensive techniques, including Adversarially Training (AT) and pre-processing based methods, such as Bit-depth Reduction (Bit-Red) [Xu et al \(2018\)](#), Neural Representation Purifier (NRP) [Naseer et al \(2020\)](#) and Diffusion Purifier (DiffPure) [Nie et al \(2022\)](#). For attacking AT models pre-trained on ImageNet, we adopt adversarially trained ResNet-50 as the surrogate model and the more powerful classifier Wide-ResNet-50-2 as the victim model [Salman et al \(2020\)](#). For other defensive techniques, we use them to process AEs from ImageNet generated for attacking standardly trained ResNet-18, and then evaluate the ASR of these AEs after being processed. The experimental results shown in Table 7 show case that Our DifAttack++ achieves the highest average ASR among the current four advanced defensive techniques, surpassing the second-place MCGSquare by nearly 10%. DifAttack++ is also the only method among the comparison methods with an average ASR exceeding 50%. Furthermore, DifAttack++ obtains two first places and two second places in terms of ASR. These results indicate that the AEs generated by DifAttack++ are more effective in resisting various types of defense mechanisms compared to other attack methods, and demonstrate the ability of DifAttack++ to

effectively decouple adversarial features from adversarially trained models. Looking back at Fig. 2, the adversarial perturbations generated by MCGSquare consist mainly of colorful blocks, which differ from conventional adversarial noise patterns. Consequently, MCGSquare exhibits significant effectiveness against defense mechanisms that focus solely on perturbations created by gradient-based attacks, such as traditional adversarial training, and techniques like the DiffPure that employ diffusion models for denoising. The aforementioned two defensive techniques primarily operate at the pixel level, whereas methods like NRP that perform denoising in deep feature space show promising results against MCGSquare, reducing its ASR to as low as 10%. In contrast, our DifAttack++ still achieve a highest ASR of 48%. Note that to be consistent with previous works [Cheng et al \(2019\)](#); [Feng et al \(2022\)](#), and due to the poor performance, the evaluation of targeted attacks under defense is temporarily omitted.

4.5 Analysis on Disentangled Features

To gain a more intuitive understanding of the characteristics of VFs and AFs disentangled by our method, we conduct an experiment to observe the changes on reconstructed images by exchanging the VFs and AFs of a pair of images.

Specifically, we exemplify applying a well pre-trained autoencoder \mathcal{G} to reconstruct and disentangle clean images \mathbf{x}_1 and \mathbf{x}_2 , resulting in their respective reconstructed images ($\tilde{\mathbf{x}}_1$ and $\tilde{\mathbf{x}}_2$) along with their VFs and AFs. Next, we input \mathbf{x}_1 's VFs and \mathbf{x}_2 's AFs into the feature fusion layer \mathbf{M} of \mathcal{G} , obtaining the mixed image $\tilde{\mathbf{x}}_{v1a2}$. Similarly, using \mathbf{x}_1 's AFs and \mathbf{x}_2 's VFs, we have $\tilde{\mathbf{x}}_{v2a1}$.

As shown in Fig. 4, we randomly select three samples from the test dataset to visualize this process. Notably, the visual quality of the reconstructed images is predominantly influenced by VFs, with minimal impact from AFs. For instance, when the VFs used for reconstructing an image originate from \mathbf{x}_1 , the reconstructed image (i.e., $\tilde{\mathbf{x}}_1$ and $\tilde{\mathbf{x}}_{v1a2}$) closely resembles \mathbf{x}_1 in visual quality no matter where their AFs come from. Similarly, VFs from \mathbf{x}_2 yield $\tilde{\mathbf{x}}_2$ and $\tilde{\mathbf{x}}_{v2a1}$, which closely resemble \mathbf{x}_2 . On the other hand, by observing the residual in reconstructed images when only AFs are replaced while keeping VFs constant (i.e., $\tilde{\mathbf{x}}_1 - \tilde{\mathbf{x}}_{v1a2}$ and $\tilde{\mathbf{x}}_2 - \tilde{\mathbf{x}}_{v2a1}$), we find that AFs significantly influence the region of category-specific objects in the reconstructed images, akin to the classifier's attention. For example, in the first row of samples, when $\tilde{\mathbf{x}}_{v1a2}$'s AFs come from \mathbf{x}_2 , the residual image $\tilde{\mathbf{x}}_1 - \tilde{\mathbf{x}}_{v1a2}$ focuses on the "black stork" object, which corresponds

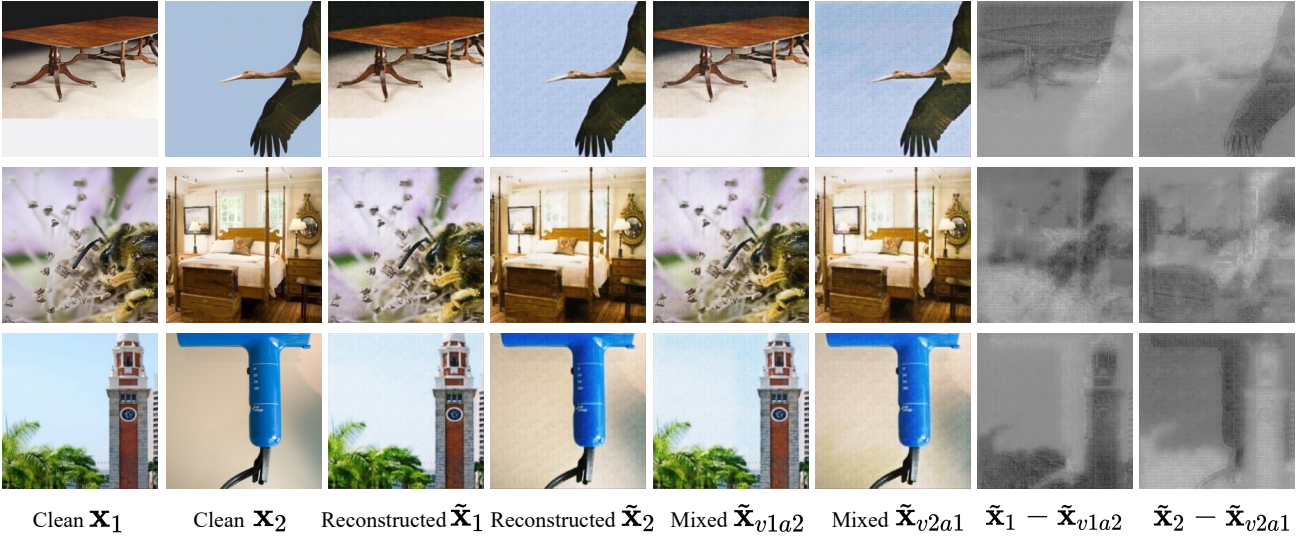


Fig. 4: The visualization of disentangled performance of visual and adversarial features. Images $\tilde{\mathbf{x}}_1$ and $\tilde{\mathbf{x}}_2$ are the reconstructed version of \mathbf{x}_1 and \mathbf{x}_2 respectively by our pretrained autoencoder \mathcal{G} . The image $\tilde{\mathbf{x}}_{v1a2}$ are reconstructed by \mathcal{G} using the VFs of \mathbf{x}_1 and the AFs of \mathbf{x}_2 , while $\tilde{\mathbf{x}}_{v2a1}$ are reconstructed by \mathcal{G} using the VFs of \mathbf{x}_2 and the AFs of \mathbf{x}_1 .

Table 8: The ablation study on the usage of cross domain (CD), the HDF module, and a transferable AE $\hat{\mathbf{x}}_T$ as the initial image in the attack stage.

Victims	GoogleNet				ResNet18				VGG16				SqueezeNet				Average			
	Targeted		Untargeted		Targeted		Untargeted		Targeted		Untargeted		Targeted		Untargeted		Targeted		Untargeted	
Settings	ASR	Avg.Q	ASR	Avg.Q	ASR	Avg.Q	ASR	Avg.Q	ASR	Avg.Q	ASR	Avg.Q	ASR	Avg.Q	ASR	Avg.Q	ASR	Avg.Q	ASR	Avg.Q
DifAttack	97.0%	3,201	100.0%	165	100.0%	1,901	100.0%	156	100.0%	2,246	100.0%	123	98.0%	2,793	100.0%	90	98.8%	2,535	100.0%	134
Dif+CD	98.0%	3,018	100.0%	177	100.0%	1,916	100.0%	137	100.0%	2,104	100.0%	<u>53</u>	99.0%	2,430	100.0%	78	99.3%	2,367	100.0%	111
Dif+CD+HDF	98.5%	2,847	100.0%	<u>133</u>	100.0%	1,685	100.0%	<u>120</u>	100.0%	1,825	100.0%	60	99.0%	2,242	100.0%	<u>55</u>	99.4%	2,150	100.0%	92
Dif+CD+HDF+$\hat{\mathbf{x}}_T$	99.5%	1,530	100.0%	80	100.0%	957	100.0%	62	100.0%	969	100.0%	52	99.0%	1,389	100.0%	41	99.6%	1,211	100.0%	58

to the brightest area (large pixel values) in the image $\tilde{\mathbf{x}}_1 - \tilde{\mathbf{x}}_{v1a2}$. Conversely, when $\tilde{\mathbf{x}}_{v2a1}$'s AFs come from \mathbf{x}_1 , the changes concentrate on the “dining table” object (highlighted in $\tilde{\mathbf{x}}_2 - \tilde{\mathbf{x}}_{v2a1}$). This phenomenon is also similarly evident in the other two rows of samples.

Based on the experimental results and analysis above, we can draw two conclusions: 1) Our DifAttack++ effectively disentangles the VFs and AFs of images. 2) VFs primarily determine the visual quality of images, and are mainly dependent on images' signals themselves, while AFs are more associated with the attention regions of the classifier and relatively independent on images' signals.

4.6 Ablation Studies

In this subsection, we conduct ablation experiments on three key improvements introduced in our proposed DifAttack++ method compared to our previous work DifAttack: 1) the training stage transitioned from using a single autoencoder for both clean images and AEs

to two separate autoencoders for clean and adversarial domains. This Cross Domain is denoted as **CD**; 2) the decoupling module within the autoencoder changed from a single-layer decouple-fusion (DF) module to a **HDF** module; and 3) the initial images at the attack stage shifted from clean samples to transferable AEs in close-set scenarios, namely from \mathbf{x} to $\hat{\mathbf{x}}_T$ generated by SI-NI-TI-DIM. The evaluation results of these upgrades are summarized in Table 8. To assess the advantages of CD, we maintain the autoencoder architecture used in DifAttack and retaining clean initial images, while adopting two autoencoders responsible for clean and adversarial domains separately, denoted as Dif+CD. Subsequently, to evaluate the HDF, we replace the DF in each autoencoder of Dif+CD with HDF, denoted as Dif+CD+HDF. Finally, to assess the gain of transferable AEs, we replace the clean initial images \mathbf{x} in Dif+CD+HDF with the AE $\hat{\mathbf{x}}_T$, representing our ultimate DifAttack++ method used in closed-set scenarios.

Table 8 shows that the three new upgrades proposed in DifAttack++ effectively enhance the ASR and query

efficiency when attacking different victim models. Consequently, we can infer the following: 1) distinguishing between clean and adversarial domains helps autoencoders focus more on learning and disentangling image features in the current domain without confusion from the other domain's distribution; 2) HDF provides more independent disentangled features compared to single-layer DF; 3) utilizing AFs of transferable AEs as a starting point can more efficiently identify successful AFs compared to using AFs from clean samples.

5 Conclusion

This work presents a novel score-based black-box attack method named DifAttack++, which aims to hierarchically disentangle the adversarial and visual features from an image's latent feature and perform black-box attacks via the disentangled feature space and cross domain. The main idea is to optimize the adversarial feature while keeping the visual feature unchanged until a successful AE is obtained. Experimental results demonstrate the superior attack efficiency of DifAttack++ in both close-set and open-set scenarios, as well as against a real-world API, meanwhile maintaining a satisfactory visual quality of AEs.

5.1 Acknowledgements

References

- Achille A, Soatto S (2018) Information dropout: Learning optimal representations through noisy computation. *IEEE transactions on pattern analysis and machine intelligence* 40(12):2897–2905
- Al-Dujaili A, O'Reilly UM (2020) Sign bits are all you need for black-box attacks. In: *Proc. Int. Conf. Learn. Representat.*
- Alemi AA, Fischer I, Dillon JV, Murphy K (2016) Deep variational information bottleneck. In: *Proc. Int. Conf. Learn. Representat.*
- Andriushchenko M, Croce F, Flammarion N, Hein M (2020) Square attack: a query-efficient black-box adversarial attack via random search. In: *Proc. Eur. Conf. Comput. Vis.*, Springer, pp 484–501
- Arora J, Tushir M, Kherwa P, Rathee S (2023) Generative adversarial networks: A comprehensive review. *Data Wrangling: Concepts, Applications and Tools* p 213
- Barbu A, Mayo D, Alverio J, Luo W, Wang C, Gutfreund D, Tenenbaum J, Katz B (2019) Objectnet: A large-scale bias-controlled dataset for pushing the limits of object recognition models. *Proc Int Conf Neural Inf Process Sys* 32
- Bengio Y, Courville A, Vincent P (2013) Representation learning: A review and new perspectives. *IEEE transactions on pattern analysis and machine intelligence* 35(8):1798–1828
- Bossard L, Guillaumin M, Van Gool L (2014) Food-101—mining discriminative components with random forests. In: *Proc. Eur. Conf. Comput. Vis.*, Springer, pp 446–461
- Brendel W, Rauber J, Bethge M (2018) Decision-based adversarial attacks: Reliable attacks against black-box machine learning models. In: *Proc. Int. Conf. Learn. Representat.*
- Burgess CP, Higgins I, Pal A, Matthey L, Watters N, Desjardins G, Lerchner A (2018) Understanding disentangling in beta-VAE. *arXiv preprint arXiv:180403599*
- Cai R, Li Z, Wei P, Qiao J, Zhang K, Hao Z (2019) Learning disentangled semantic representation for domain adaptation. In: *IJCAI: proceedings of the conference, NIH Public Access*, vol 2019, p 2060
- Cai Z, Song C, Krishnamurthy S, Roy-Chowdhury A, Asif S (2022) Blackbox attacks via surrogate ensemble search. In: *Proc. Int. Conf. Neural Inf. Process. Sys.*, vol 35, pp 5348–5362
- Carlini N, Wagner D (2017) Towards evaluating the robustness of neural networks. In: *Proc. IEEE Conf. Symp. Security Privacy.*, pp 39–57
- Chen H, Zhang Y, Wu S, Wang X, Duan X, Zhou Y, Zhu W (2024) Disenbooth: Identity-preserving disentangled tuning for subject-driven text-to-image generation. In: *Proc. Int. Conf. Learn. Representat.*
- Chen RT, Li X, Grosse RB, Duvenaud DK (2018) Isolating sources of disentanglement in variational autoencoders. *Proc Int Conf Neural Inf Process Sys* 31
- Chen X, Duan Y, Houthoofd R, Schulman J, Sutskever I, Abbeel P (2016) Infogan: Interpretable representation learning by information maximizing generative adversarial nets. In: *NeurIPS*
- Cheng S, Dong Y, Pang T, Su H, Zhu J (2019) Improving black-box adversarial attacks with a transfer-based prior. In: *Proc. Int. Conf. Neural Inf. Process. Sys.*, vol 32
- Choi S, Lee S, Kim Y, Kim T, Kim C (2020) Hicmd: Hierarchical cross-modality disentanglement for visible-infrared person re-identification. In: *Proc. IEEE Conf. Comput. Vis. Pattern Recogn.*, pp 10257–10266
- Croce F, Hein M (2020a) Minimally distorted adversarial examples with a fast adaptive boundary attack. In: *Proc. Int. Conf. Mach. Learn.*, PMLR, pp 2196–2205

- Croce F, Hein M (2020b) Reliable evaluation of adversarial robustness with an ensemble of diverse parameter-free attacks. In: Proc. Int. Conf. Mach. Learn., pp 2206–2216
- Deng J, Dong W, Socher R, Li LJ, Li K, Fei-Fei L (2009) Imagenet: A large-scale hierarchical image database. In: Proc. IEEE Conf. Comput. Vis. Pattern Recogn., IEEE, pp 248–255
- Dong Y, Liao F, Pang T, Su H, Zhu J, Hu X, Li J (2018) Boosting adversarial attacks with momentum. In: Proc. IEEE Conf. Comput. Vis. Pattern Recogn., pp 9185–9193
- Dong Y, Fu QA, Yang X, Pang T, Su H, Xiao Z, Zhu J (2020) Benchmarking adversarial robustness on image classification. In: Proc. IEEE Conf. Comput. Vis. Pattern Recogn., pp 321–331
- Du J, Zhang H, Zhou JT, Yang Y, Feng J (2020) Query-efficient meta attack to deep neural networks. In: Proc. Int. Conf. Learn. Representat.
- Feng Y, Wu B, Fan Y, Liu L, Li Z, Xia ST (2022) Boosting black-box attack with partially transferred conditional adversarial distribution. In: Proc. IEEE Conf. Comput. Vis. Pattern Recogn., pp 15095–15104
- Gadre SY, Ilharco G, Fang A, Hayase J, Smyrnis G, Nguyen T, Marten R, Wortsman M, Ghosh D, Zhang J, et al (2024) Datacomp: In search of the next generation of multimodal datasets. Proc Int Conf Neural Inf Process Sys 36
- Gao G, Huang H, Fu C, Li Z, He R (2021) Information bottleneck disentanglement for identity swapping. In: Proc. IEEE Conf. Comput. Vis. Pattern Recogn., pp 3404–3413
- Gonzalez-Garcia A, Van De Weijer J, Bengio Y (2018) Image-to-image translation for cross-domain disentanglement. Proc Int Conf Neural Inf Process Sys 31
- Goodfellow I, Pouget-Abadie J, Mirza M, Xu B, Warde-Farley D, Ozair S, Courville A, Bengio Y (2014) Generative adversarial nets. In: Proc. Int. Conf. Neural Inf. Process. Sys., vol 27
- Google (2024) Google cloud vision api. <https://cloud.google.com/vision>, accessed:2023-08-15
- Guo C, Rana M, Cisse M, van der Maaten L (2018) Countering adversarial images using input transformations. In: Proc. Int. Conf. Learn. Representat.
- Guo C, Gardner J, You Y, Wilson AG, Weinberger K (2019a) Simple black-box adversarial attacks. In: Proc. Int. Conf. Mach. Learn., pp 2484–2493
- Guo Y, Yan Z, Zhang C (2019b) Subspace attack: Exploiting promising subspaces for query-efficient black-box attacks. In: Proc. Int. Conf. Neural Inf. Process. Sys., vol 32
- Higgins I, Matthey L, Pal A, Burgess C, Glorot X, Botvinick M, Mohamed S, Lerchner A (2017) beta-vae: Learning basic visual concepts with a constrained variational framework. In: Proc. Int. Conf. Learn. Representat.
- Hinton GE, Zemel R (1993) Autoencoders, minimum description length and helmholtz free energy. In: Proc. Int. Conf. Neural Inf. Process. Sys., vol 6
- Huang Z, Zhang T (2020) Black-box adversarial attack with transferable model-based embedding. In: Proc. Int. Conf. Learn. Representat.
- Ilharco G, Wortsman M, Wightman R, Gordon C, Carlini N, Taori R, Dave A, Shankar V, Namkoong H, Miller J, Hajishirzi H, Farhadi A, Schmidt L (2021) Openclip. DOI 10.5281/zenodo.5143773, URL <https://doi.org/10.5281/zenodo.5143773>, if you use this software, please cite it as below.
- Ilyas A, Engstrom L, Athalye A, Lin J (2018) Black-box adversarial attacks with limited queries and information. In: Proc. Int. Conf. Mach. Learn., pp 2137–2146
- Imagga (2024) Ai-powered image tagging api. "<https://imagga.com/solutions/auto-tagging>", accessed:2023-08-15
- Kim H, Mnih A (2018) Disentangling by factorising. In: Int. Conf. on Machine Learn., PMLR, pp 2649–2658
- Kim J, Lee BK, Ro YM (2021) Distilling robust and non-robust features in adversarial examples by information bottleneck. In: Proc. Int. Conf. Neural Inf. Process. Sys., vol 34, pp 17148–17159
- Lee HY, Tseng HY, Huang JB, Singh M, Yang MH (2018a) Diverse image-to-image translation via disentangled representations. In: Proc. Eur. Conf. Comput. Vis., pp 35–51
- Lee HY, Tseng HY, Mao Q, Huang JB, Lu YD, Singh MK, Yang MH (2020) Dri++: Diverse image-to-image translation via disentangled representations. Inter Journal of Comput Vis pp 1–16
- Lee K, Lee K, Lee H, Shin J (2018b) A simple unified framework for detecting out-of-distribution samples and adversarial attacks. Proc Int Conf Neural Inf Process Sys 31
- Li P, Pei Y, Li J (2023) A comprehensive survey on design and application of autoencoder in deep learning. Applied Soft Computing p 110176
- Li Y, Li L, Wang L, Zhang T, Gong B (2019) Nat-tack: Learning the distributions of adversarial examples for an improved black-box attack on deep neural networks. In: Proc. Int. Conf. Mach. Learn., pp 3866–3876
- Lin CC, Chu HL, Wang YCF, Lei CL (2021) Joint feature disentanglement and hallucination for few-shot image classification. IEEE Transactions on Image Processing 30:9245–9258
- Lin J, Song C, He K, Wang L, Hopcroft JE (2019) Nesterov accelerated gradient and scale invariance for

- adversarial attacks. In: International Conference on Learning Representations
- Lin WA, Lau CP, Levine A, Chellappa R, Feizi S (2020) Dual manifold adversarial robustness: Defense against lp and non-lp adversarial attacks. *Proc Int Conf Neural Inf Process Sys* 33:3487–3498
- Liu J, Zhou J, Zeng J, Tian J (2024a) Difattack: Query-efficient black-box attack via disentangled feature space. In: *Proceedings of the AAAI Conference on Artificial Intelligence*, vol 38, pp 3666–3674, DOI 10.1609/aaai.v38i4.28156, URL <https://ojs.aaai.org/index.php/AAAI/article/view/28156>
- Liu R, Zhou W, Zhang T, Chen K, Zhao J, Lam KY (2024b) Boosting black-box attack to deep neural networks with conditional diffusion models. *IEEE Trans Inf Forensics and Security*
- Lord NA, Mueller R, Bertinetto L (2022) Attacking deep networks with surrogate-based adversarial black-box methods is easy. In: *Proc. Int. Conf. Learn. Representat.*
- Lu S, Xian Y, Yan K, Hu Y, Sun X, Guo X, Huang F, Zheng WS (2021) Discriminator-free generative adversarial attack. In: *Proc. ACM Int. Conf. Multimedia.*, pp 1544–1552
- Ma X, Kong X, Zhang S, Hovy EH (2020) Decoupling global and local representations via invertible generative flows. In: *Proc. Int. Conf. Learn. Representat.*
- Madry A, Makelov A, Schmidt L, Tsipras D, Vladu A (2018) Towards deep learning models resistant to adversarial attacks. In: *Proc. Int. Conf. Learn. Representat.*
- Meo C, Mahon L, Goyal A, Dauwels J (2024) α tc-vae: On the relationship between disentanglement and diversity. In: *Proc. Int. Conf. Learn. Representat.*
- Mohaghegh Dolatabadi H, Erfani S, Leckie C (2020) Advflow: Inconspicuous black-box adversarial attacks using normalizing flows. In: *Proc. Int. Conf. Neural Inf. Process. Sys.*, pp 15871–15884
- Mustafa A, Khan SH, Hayat M, Goecke R, Shen J, Shao L (2020) Deeply supervised discriminative learning for adversarial defense. *IEEE Trans on Pattern Anal and Mach Intell* 43(9):3154–3166
- Naseer M, Khan S, Hayat M, Khan FS, Porikli F (2020) A self-supervised approach for adversarial robustness. In: *Proc. IEEE Conf. Comput. Vis. Pattern Recogn.*, pp 262–271
- Nie W, Guo B, Huang Y, Xiao C, Vahdat A, Anandkumar A (2022) Diffusion models for adversarial purification. In: *Proc. Int. Conf. Mach. Learn.*
- Peng X, Huang Z, Sun X, Saenko K (2019) Domain agnostic learning with disentangled representations. In: *Int. Conf. on Machine Learn.*, PMLR, pp 5102–5112
- Pope P, Zhu C, Abdelkader A, Goldblum M, Goldstein T (2020) The intrinsic dimension of images and its impact on learning. In: *Proc. Int. Conf. Learn. Representat.*
- Qin Y, Xiong Y, Yi J, Hsieh CJ (2023) Training meta-surrogate model for transferable adversarial attack. In: *Proc. of the AAAI Conf. on Artif. Intell.*, vol 37, pp 9516–9524
- Qing Y, Bai T, Liu Z, Moulin P, Wen B (2024) Detection of adversarial attacks via disentangling natural images and perturbations. *IEEE Trans Inf Forensics and Security*
- Salman H, Ilyas A, Engstrom L, Kapoor A, Madry A (2020) Do adversarially robust imagenet models transfer better? **2007.08489**
- Stutz D, Hein M, Schiele B (2019) Disentangling adversarial robustness and generalization. In: *Proc. IEEE Conf. Comput. Vis. Pattern Recogn.*, pp 6976–6987
- Tong B, Wang C, Klinkigt M, Kobayashi Y, Nonaka Y (2019) Hierarchical disentanglement of discriminative latent features for zero-shot learning. In: *Proc. IEEE Conf. Comput. Vis. Pattern Recogn.*, pp 11467–11476
- Vaze S, Han K, Vedaldi A, Zisserman A (2021) Open-set recognition: A good closed-set classifier is all you need. In: *Proc. Int. Conf. Learn. Representat.*
- Wang S, Nepal S, Rudolph C, Grobler M, Chen S, Chen T, An Z (2021) Defending adversarial attacks via semantic feature manipulation. *IEEE Trans on Serv Comput* 15(6):3184–3197
- Wang X, Chen H, Tang S, Wu Z, Zhu W (2022) Disentangled representation learning. *arXiv preprint arXiv:221111695*
- Wei Z, Yang X, Wang N, Gao X (2023) Dual-adversarial representation disentanglement for visible infrared person re-identification. *IEEE Trans Inf Forensics and Security*
- Wierstra D, Schaul T, Glasmachers T, Sun Y, Peters J, Schmidhuber J (2014) Natural evolution strategies. *The Journal of Mach Learn Resear* 15(1):949–980
- Xu W, Evans D, Qi Y (2018) Feature squeezing: Detecting adversarial examples in deep neural networks. In: *Proc. Netw. Distrib. Syst. Secur. Symp.*
- Yang K, Zhou T, Zhang Y, Tian X, Tao D (2021a) Class-disentanglement and applications in adversarial detection and defense. *Proc Int Conf Neural Inf Process Sys* 34:16051–16063
- Yang S, Guo T, Wang Y, Xu C (2021b) Adversarial robustness through disentangled representations. In: *Proc. of the AAAI Conf. on Artif. Intell.*, vol 35, pp 3145–3153
- Yang T, Wang Y, Lu Y, Zheng N (2024) Disdiff: Unsupervised disentanglement of diffusion probabilistic

- models. Proc Int Conf Neural Inf Process Sys 36
- Yin F, Zhang Y, Wu B, Feng Y, Zhang J, Fan Y, Yang Y (2023a) Generalizable black-box adversarial attack with meta learning. IEEE Trans on Pattern Anal and Mach Intell pp 1–13
- Yin F, Zhang Y, Wu B, Feng Y, Zhang J, Fan Y, Yang Y (2023b) Generalizable black-box adversarial attack with meta learning. IEEE Trans on Pattern Anal and Mach Intell
- Zhang H, Avrithis Y, Furon T, Amsaleg L (2021) Walking on the edge: Fast, low-distortion adversarial examples. IEEE Trans Inf Forensics and Security 16:701–713
- Zhu JY, Park T, Isola P, Efros AA (2017) Unpaired image-to-image translation using cycle-consistent adversarial networks. In: Proc. IEEE Conf. Comput. Vis.